sustainability

MDPI

Article

Coupling Study of Deformation Field Evolution and Acoustic Emission Response Characteristics in Rock Failure and Instability Process

Zhengxing Yu [1], Quanjie Zhu [2,*], Erhui Zhang [3], Yihai Zhang [1], Lei Gu [4], Longkun Sui [4] and Yongming Yin [1]

[1] China Academy of Safety Science and Technology, Beijing 100012, China
[2] School of Emergency Technology and Management, North China Institute of Science and Technology, Beijing 101601, China
[3] School of Mechanics and Civil Engineering, China University of Mining & Technology (Beijing), Beijing 100083, China
[4] School of Mine Safety, North China Institute of Science and Technology, Beijing 101601, China
* Correspondence: youyicun2008@163.com; Tel.: +86-137-1845-9909

check for updates

Citation: Yu, Z.; Zhu, Q.; Zhang, E.; Zhang, Y.; Gu, L.; Sui, L.; Yin, Y. Coupling Study of Deformation Field Evolution and Acoustic Emission Response Characteristics in Rock Failure and Instability Process. *Sustainability* **2022**, *14*, 15037. https://doi.org/10.3390/su142215037

Academic Editors: Kai Wang, Yubing Liu and Xiaojun Feng

Received: 3 October 2022
Accepted: 9 November 2022
Published: 14 November 2022

Abstract: During rock failure and instability, cracks usually appear as microcracks in local areas and then expand into significant macroscopic cracks. In this study, the whole process of rock deformation and instability under uniaxial loading is investigated with standard rock specimens, and acoustic emission (AE) and digital image correlation (DIC) technology are introduced to explore the process of rock failure and instability. AE technology is used to identify the location of crack propagation caused by microcracks and large cracks, and DIC is used to measure the crack propagation at different locations. Results show that the evolution of accumulated energy is closely related to the change in stress. When the specimen approaches failure, a "y" shaped localization zone is formed, and the evolution path is consistent with the through-through path of the crack, which better reflects the propagation law of the crack in the rock. The spatial distribution of the AE location event and energy density is consistent with the evolution path of the localization zone. The deformation value of the deformation field is closely related to the initiation and evolution of the deformation localization zone. On the basis of density-based spatial clustering of applications with a noise-clustering algorithm, AE positioning events are further processed and projected into the digital image of the deformation field, and the results of clustering projection are in good agreement with the deformation localization zone. Results show that AE and DIC coupling localization techniques can effectively identify the fracture process zone and fracture mechanism of rock, providing a new technical means for further studying the mechanical properties of rock materials.

Keywords: rock mechanics; instability failure; deformation field; digital image correlation; acoustic emission; DBSCAN clustering

1. Introduction

Mining activities under a high-stress environment are prone to the deformation and instability of the surrounding rock and induce engineering disasters, such as rock bursts, because of the influence of geological structures and excavation disturbances. In recent years, frequent dynamic mine disasters have posed a great threat to the safety of coal mine production and the safety of the majority of coalmine workers. Mastering the failure mechanism of rock is of great importance to realize the safe production of mines and reduce the accident rate.

Mining activities under high stresses are affected by geological structures and excavation disturbances and easily cause the deformation instability of surrounding rock, thereby inducing rock-burst disasters. The transient electromagnetic method is a good choice for geological structure detection. The identification of geological anomalies can be preliminarily realized by using microseismic technology [1,2]. When a rock is damaged and destroyed under external forces, the evolution of its internal microcracks is consistent with the failure process. In the destruction process, the energy gathered inside is mainly released in the form of elastic waves, which is called "acoustic emission phenomenon" [3]. Many researchers have studied the rock instability deformation process through theoretical analysis, laboratory test, field monitoring, and numerical simulation combined with acoustic emission characteristics. As the base approach, theoretical analysis serves as a guide to explore rock instability deformation. Zou et al. derived the relationship between the acoustic emission characteristic parameters of rock and rock damage in accordance with relevant theories [4–6]. They quantitatively characterized the damage degree and failure evolution process of rock on the basis of acoustic emission characteristic parameters. On the basis of mathematical modellings, the deformation and failure characteristics of rocks can be directly reflected through laboratory test and field monitoring. Zhang et al. used integrated acoustic (AC) and acoustic emission (ACE) devices to synchronously test the rock damage evolution process under uniaxial compression in terms of crack volume strain, ACE, and AC characteristics [7]. Zuo et al. found the differences in failure mechanisms between the rock, coal, and coal–rock combination under uniaxial compression by means of ACE tests [8]. Li Shulin et al. conducted an ACE test on rock in the whole process of uniaxial compression and found the mechanical characteristics and ACE characteristics in the process of rock failure [9]. The ACE and the failure characteristics of rocks are reported through on-site monitoring [10–12]. Combined with theoretical analysis and laboratory and field test data, the dynamic process of coal and rock failure can be visualized via numerical simulation. Zhou et al. combined the experimental results of ACE characteristics in the whole process of rock failure on laboratory scale [13–15]. They confirmed that the numerical simulation is valid and accurate for revealing the failure mechanism of coal and rock.

The ACE method can accurately determine the fracture location, but it has disadvantages in characterizing the deformation field after failure. Therefore, it is necessary to discuss and verify the deformation field by other means. In laboratory tests, the DIC method is often used to quantitatively describe the deformation field. DIC technology can only detect the surface deformation of the specimen and cannot obtain the internal changes of the specimen. Therefore, the combination of ACE and DIC detection can realize the 'internal–external' simultaneous detection of the specimen loading-failure process and better characterize the failure law of the specimen. The digital image correlation (DIC) method is a deformation field test method based on digital image processing. It is considered as a method with advantages of being full field, non-contact, high precision, sensitive measurement, large range, and easy to implement [16]. The DIC method is becoming more and more common and has been widely used to investigate coal properties [17], concrete [18], aluminum alloy [19], stainless steel [20], and deformation testing of rock-like materials. Munoz et al. studied the evolution characteristics and energy of the deformation field during rock failure and instability under various loading states such as uniaxial, cyclic loading, and compression–tension cycles release rules [21,22]. Ma et al. used the three-dimensional DIC method to study the whole process of granite slab failure with central circular holes under uniaxial compression [23,24]. Zhao et al. conducted an experimental study on the effect of three-dimensional roughness of rock fractures on seepage characteristics by means of the DIC method [25]. In addition, the evolution characteristics of rock deformation and damage from the mesoscopic level also could be found by the DIC method, as reported by [26].

A large number of studies have revealed the failure characteristics of rocks from the single aspects of rock mechanics analysis, ACE characteristics, and deformation field evolution characteristics. However, a direct relationship is observed between the internal damage and evolution of surface deformation field in the unstable failure process of rock. Few studies are reported on the failure mechanism of rock specimens combined with ACE localization and evolution characteristics of a digital image correction (DIC) surface deformation field. In this study, standard rock specimens are used for a uniaxial compression test, and a charge-coupled device (CCD) camera and an ACE system are applied to collect the deformation image of the specimen surface and the ACE signal inside the specimen. The ACE response characteristics and evolution characteristics of the deformation field during rock failure and instability are investigated by combining the DIC method and ACE signal.

2. Analysis of Rock Failure Instability Mechanism Based on Multifield Monitoring

Rock failure is triggered by localized deformation [27]. The study of a rock failure process from the perspective of deformation localization has become a hot issue in rock mechanics research [28]. At present, ACE and DIC are the two most effective methods for rock failure process characterizations.

The purpose of DIC is to obtain parameters, such as displacement and deformation, by calculating the grayscale of a speckle image before and after specimen surface deformation. The feature functions of the pre-warped base image and the post-warped target image are given as $I1 = F1(x, y)$ and $I2 = F2(x, y)$ to evaluate the deformation features between the reference region and the deformed region, respectively. Assuming that the position of point P on the reference image is tracked, the matching point must be obtained on the target image. A square reference subarea is selected in the reference image before deformation, and a point-by-point search for the corresponding displacement value on the target image after deformation is performed. A correlation matching method is used to search for the most-matching digital image subregion on the deformed target image. The displacement of point P is obtained when the matching is successful [23]. The full strain field of monitoring area is obtained by using this method. The principle of DIC is shown in Figure 1.

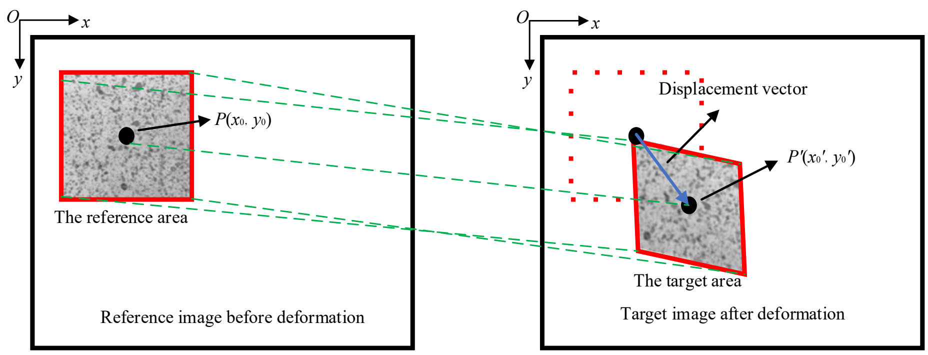

Figure 1. Schematic diagram of digital image correlation match [29].

The ACE technology with a dynamic nondestructive testing can determine the ACE source location and analyze the ACE source properties. The ACE can also determine the time and energy when the ACE source occurs. The ACE test can only obtain the microscopic evolution characteristics of the cracks and internal fracture area of specimens. However, it cannot accurately reflect the failure and instability process of rocks unless it is performed by using nondestructive testing methods for re-examination. The DIC can realize high-precision measurement on field surface displacement, intuitively reflecting the crack initiation position and spatial evolution characteristics of macroscopic cracks. However, the DIC is limited to the specimen surface and cannot really represent the number of cracks inside the specimen, and the unreachable areas are still unknown. DIC is an effective method used to measure the surface macroscopic fracture length and crack opening. ACE monitors the width and length of the internal microscopic fracture region. The crack evolution trends described by the two techniques (ACE and DIC) are similar. The DIC can measure the crack length attributes on the specimen surface and is accurate and easy to operate. The ACE is used to determine the spatial evolution characteristics of cracks and the location of crack initiation.

In this study, the development process of rock instability failure fractures is investigated by using ACE and DIC simultaneously. These techniques allow continuous and real-time data acquisition and can provide the initiation position and spatial evolution characteristics of microcracks inside the specimen. The microscopic characteristics of rocks and the macroscopic cracks of specimen surface deformation are observed through qualitative analysis. The advantages and disadvantages of the two technologies complement each other. The failure and instability process of rock is comprehensively explored from the interior to the surface and from the macro to the microscale.

3. Test Equipment and Experimental Scheme

3.1. Equipment and Experiment Design

The test device and monitoring system are shown in Figure 2 and include three parts: a test loading system, acoustic emission system, and digital image acquisition system. An RLJW-2000 testing machine was used as the test loading system, the control method was displacement expansion, and the displacement control loading rate was 0.05 mm/min. A CCD camera and a holographic acoustic emission meter were used to build a data acquisition system for collecting speckle images and acoustic emission signals on the surface of the specimen during the whole process of loading the test. The CCD camera rate is 3.5 frames/second, the image resolution is 1600 pixels × 1200 pixels, and the object surface resolution is 0.1316 mm/pixel. The acoustic emission instrument is a DS5-8B full-information acoustic emission acquisition instrument, with a sampling frequency of 3 MHz, and it adopts a threshold trigger (100 mV) as its trigger method. The sensor was fixed to the surface of the specimen, and Vaseline was used as a couplant to increase the coupling effect between the sensor and the contact surface of the metal shell. Two sensors were arranged on each of the other three sides, except the speckle surface.

Figure 2. Test equipment and monitoring system.

The DS5-8B full-information acoustic emission acquisition instrument has eight channels, with a 3 MHz sampling frequency and a threshold trigger (100 mV) as the trigger mode. The sensor is RS-5A, with a center frequency of 150 kHz and a frequency range of 60–400 KHz. The metal shell was fixed to the surface of the specimen by a solid adhesive, and the coupling effect of the contact surface between the sensor and the metal shell was increased by the coupling agent. The sensor was fixed at the distance of 15 mm between the two ends of the specimen, and a sensor was arranged at 90° intervals in the counterclockwise direction.

The ACE test of the uniaxial loading process was conducted on five groups of specimens by using the above experimental method. Only the representative specimens R-1–4 were analyzed because of the limited space.

3.2. Test Process and Results

The loading system recorded the mechanical parameters, such as stress, strain, and time. The acoustic emission acquisition system recorded the acoustic emission characteristic parameters, such as microseismic spatial positioning events, impact numbers, ringing counts, energy, and waveform. The digital image acquisition system recorded the evolution of the surface deformation field of the specimen image. Figure 3 shows the total stress–strain curve of the specimen during the loading failure process. Six typical moments were selected through analysis. The marked points of A–F corresponded to the moments in the global rock evolution analysis below. The pore compaction stage was from the beginning of loading to the OA stage. The elastic stage, linear elastic deformation acceleration stage, plastic stage failure stage, post-peak deformation failure stage, and residual strength stage were assigned to the A–B, B–C, C–D, D–E, and E–F stages, respectively. Figure 4 compares the diagram of the specimen before and after failure.

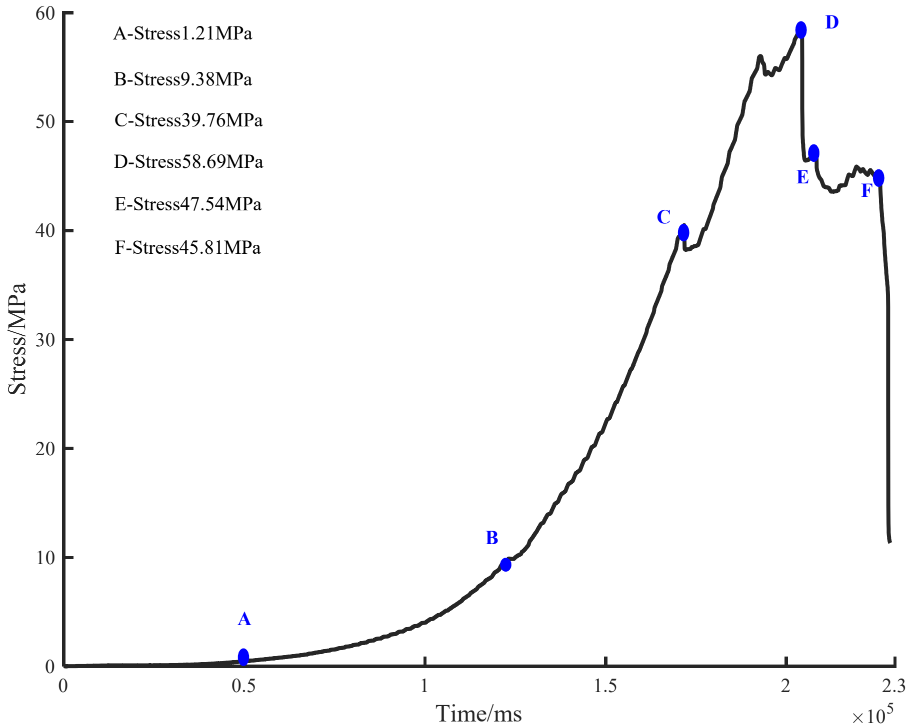

Figure 3. Full stress–strain curve during specimen loading.

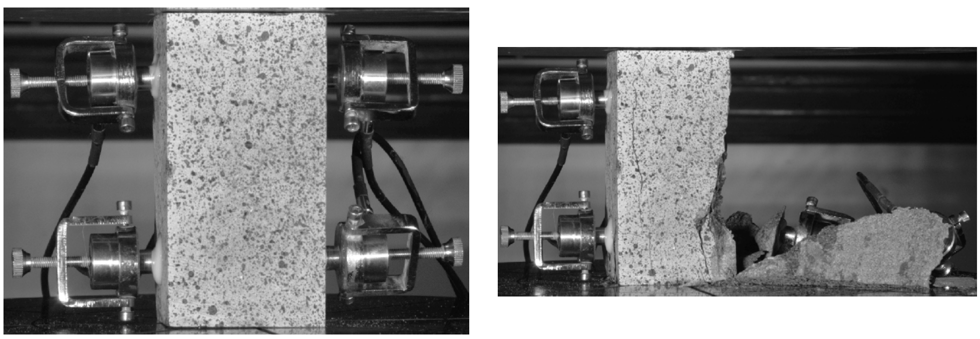

Figure 4. Comparison diagram of specimen before and after failure.

4. Analysis of Test Results

4.1. Analysis of Acoustic Emission Characteristics

In the early stage of loading, the acoustic emission response was weakened because of the effects of natural defects in the rock. The acoustic emission ringing count and acoustic emission energy indexes were small. The acoustic emission signal in the later stage of loading (plastic deformation and failure stage) was selected for analysis to determine the evolution of the acoustic emission characteristics in detail. The results of the full stress–strain curve under load and the acoustic emission response characteristics of the specimen were obtained. Six typical moments were selected as identification points to study the curves and response characteristics. The acoustic emission characteristic signal was processed and analyzed on MATLAB. The corresponding relationship between acoustic emission ringing count, acoustic emission energy, and time were obtained, as shown in Figures 5 and 6.

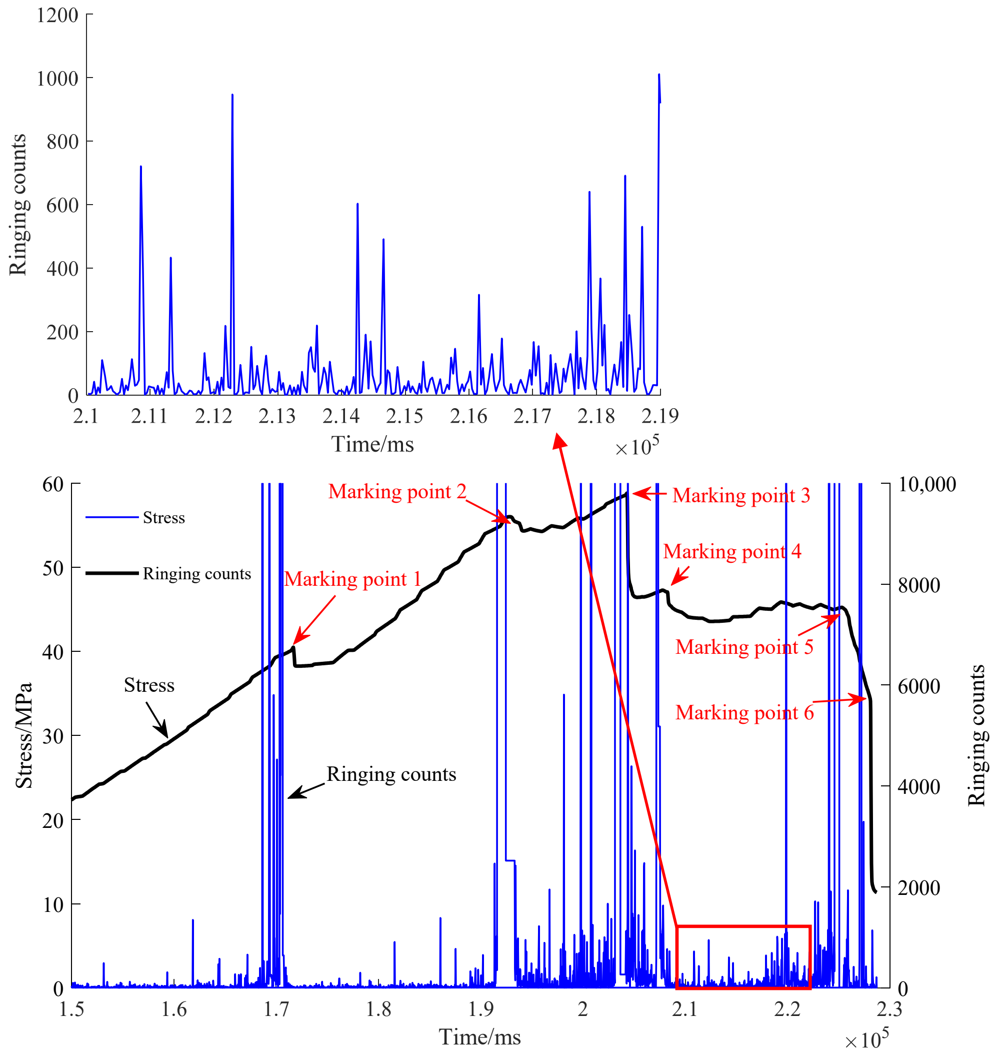

Figure 5. Stress, acoustic emission ringing count, and time relationship after loading.

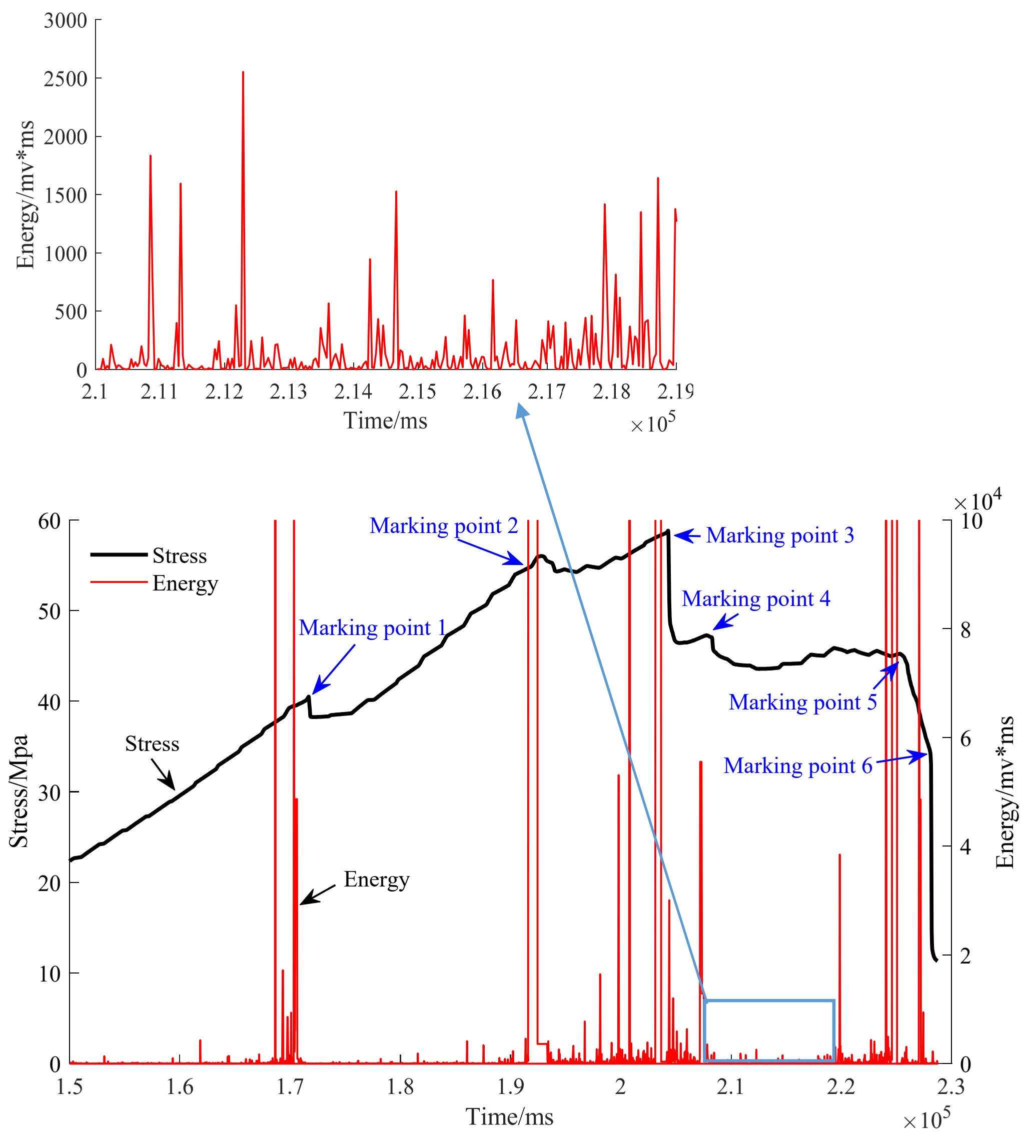

Figure 6. Stress, AE energy, and time relationship after loading.

As shown in Figures 5 and 6, the changes in stress, acoustic emission ringing count, and acoustic emission energy were similar. The stress increased linearly versus time before point 1. The acoustic emission ringing count and acoustic emission energy fluctuated slightly. At point 1, the stress dropped slightly, whereas the acoustic emission ringing count increased sharply. The stress continued to linearly increase after point 1 until the time to point 2. The acoustic emission ringing count and acoustic emission energy remained constant in this stage. The stress dropped gently at point 2. The acoustic emission ringing count and acoustic emission energy also surged. The stress first increased gently after entering the "quiet period" before the peak and then abruptly increased until the peak value. At the time of the sudden increase, the acoustic emission ringing count and acoustic emission energy also surged. The acoustic emission energy surged again. At point 4, the stress dropped again, and the acoustic emission ringing count and ACE energy surged again. After point 4, the acoustic emission energy entered the residual strength stage, and the stress dropped suddenly at points 5 and 6. The ACE ring count and ACE energy surged. Late at point 3, stress began to decline and the specimen began to be destroyed, but it did not completely lose bearing capacity; with the evolution of the stress, the specimen underwent deformation damage until it gradually completely lost bearing capacity in the process, but it was still accompanied by a large number of acoustic emission signals, so the stress time decreased significantly earlier than the acoustic emission signal.

Figure 7 shows the evolution characteristics of stress in the whole process of loading, the accumulative ringing count of the acoustic emission, and the accumulative energy of the acoustic emission with time. In the early stage of point B, the stress increased gently under the influence of natural defects in the rock. The acoustic emission response was weak, and the accumulated ringing count of the acoustic emission and the accumulated energy of the acoustic emission had no obvious changes. With the continuous increase in stress, it entered an elastic deformation stage in which the acoustic emission cumulative ringing count and cumulative energy increased linearly. Point C shown in Figure 7 corresponded to the points in Figures 5 and 6. From identification points 1 and 6, the stress change characteristics were the same as those described above. The stress at the six identification points dropped to varying degrees, and the accumulated ringing count and accumulated energy of the acoustic emission at these times greatly increased. When the stress between points 2 and 3 had a sudden increase, the accumulative ringing count and accumulative energy of the acoustic emission increased significantly. The accumulative ringing count and accumulative energy of acoustic emission increased linearly in other time periods.

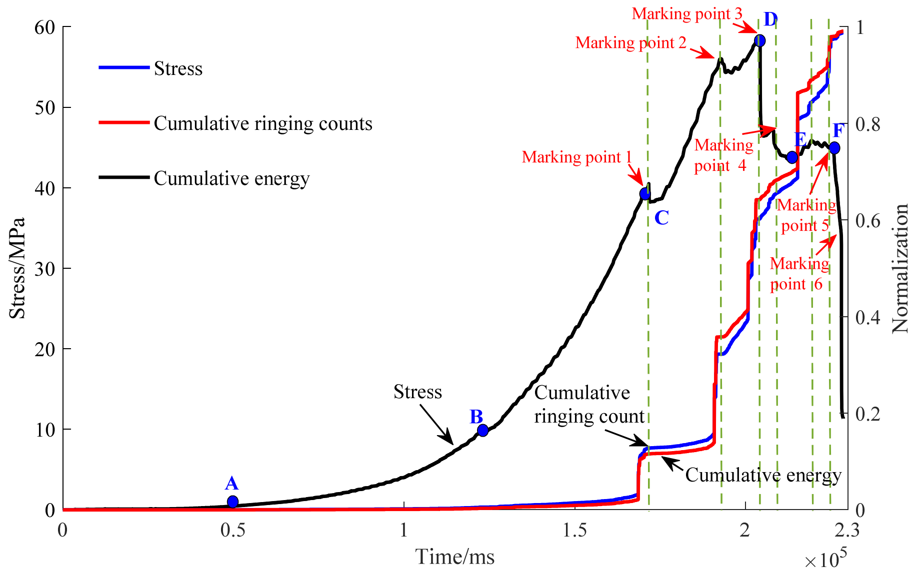

Figure 7. Characteristics of cumulative ringing count and cumulative energy evolution during uniaxial loading.

In accordance with the above analysis, the intensity of the rock acoustic emission response is closely related to the variation characteristics of stress. When the stress has a sudden change (sudden drop or surge), the acoustic emission response is violent and the acoustic emission ringing count and acoustic emission energy increase significantly. When the stress changes steadily, the acoustic emission response is weak, and the acoustic emission ringing count and acoustic emission energy decrease slightly. Some acoustic emission response characteristics may be different from the failure evolution characteristics of the specimen because of the limitations of the acoustic emission monitoring technology. Therefore, the failure and instability characteristics of the specimen must be further investigated by speckle test and the DIC method.

4.2. Analysis of the Evolution Characteristics of a Deformation Field

The characteristics of strain-field evolution, local deformation, and crack propagation during the loading process of the specimen were collected and calculated on the basis of digital speckle technology and image processing-related methods. A local deformation field was formed when the rock was loaded and deformed. The main characteristics of the local deformation field were as follows: (1) the deformation value in the deformation localized zone is larger than the deformation value outside the deformation localized zone; and (2) the points with larger deformation value are concentrated within one or more bands. The statistical index S_w was introduced to analyze the evolution process of the local deformation field and to reflect the "numerical" and "spatial" characteristics at the same time. The statistical index is expressed as:

$$S_w = w_s S \tag{1}$$

where w_s is the weight of the localized "space" feature of deformation at a certain time; and S is the variance of deformation field at a certain time. S can be expressed as:

$$S = S(X_k) = \sqrt{\frac{1}{n-1}\sum_{k=1}^{n}(X_k - \overline{X})^2} \tag{2}$$

$$w_s = S(X_k^*) = \sqrt{\frac{1}{n-1}\sum_{k=1}^{n}(X_k^* - \overline{X^*})^2} \tag{3}$$

$$\overline{X} = \frac{1}{n}\sum_{k=1}^{n} X_k \tag{4}$$

$$X^* = X \otimes B \tag{5}$$

where X_k is the deformation amount of each point in the deformation field; $\overline{X}$ is mean value of X_k; and X^* is the spatialized deformation field (deformation field data matrix), and a matrix B is used, where its elements are all 1, and its size is $m \times m$ (convolution kernel) convolution.

The value of the statistical index is calculated by using the above formula. The normalized curve of stress and its change with time were obtained, as shown in Figure 8.

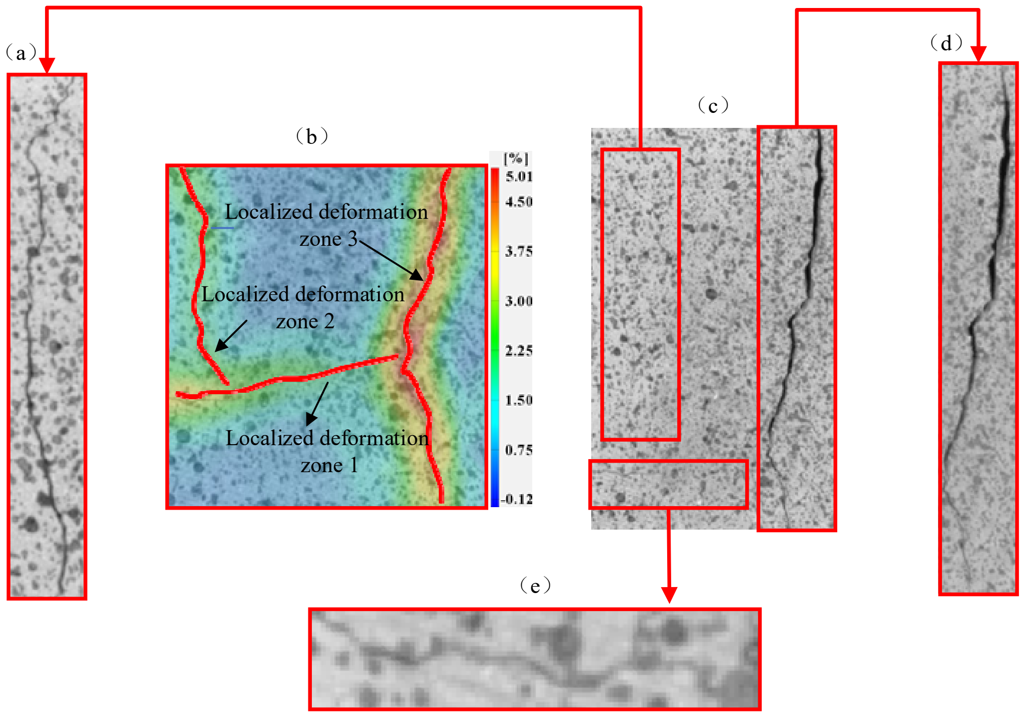

Figure 8. Deformation localization zone and crack morphology. (**a**) is localized deformation, zone 2, (**b**) is the local tensile and shear strain field, (**c**) is the overall feature map of the crack in rock matrix, (**d**) is localized deformation zone 3, (**e**) is localized deformation zone 3.

The evolution curve of the statistical index S_w in Figure 8 can be divided into three stages. The first stage corresponds to the loading time of 0–0.5 $\times$ 10^5 ms. The statistical index S_w increases linearly and smoothly, and the magnitude is small. This condition is caused by the local adjustment of the irregularity of the structure and corresponds to the pore compaction stage of the stress curve. The second stage corresponds to the loading time of 0.5 $\times$ 10^5 to 1.65 $\times$ 10^5 ms, the statistical index S_w increases exponentially, and the magnitude increases significantly. In this stage, the microcracks inside the specimen gradually develop and penetrate, and the specimen has no obvious failure characteristics, corresponding to the linear elastic deformation stage of the stress curve. The third stage corresponds to the loading time of 1.65 $\times$ 10^5 ms to the end of the loading, and the statistical index S_w fluctuates greatly. In this stage, the microcrack evolves into a macrocrack and penetrates rapidly, resulting in rock failure and instability corresponding to the plastic deformation failure stage and residual strength stage of the stress curve. The localized zone gradually evolves with the increase in stress.

Figure 8 shows the deformation localization zone and crack shape at the time of the identification point F, where (b) is the local tensile and shear strain field; T is the extension of tensile crack inside the rock; S is the extension of the shear crack inside the rock; (c) is the overall feature map of the crack in rock matrix; and (a), (d), and (e) are the enlarged views of local crack. The tensile and shear strain fields in (b) agree with the crack morphology and spatial location in (c). During the loading process of the specimen, the internal microcracks cannot be observed with the naked eye but can be identified by the strain localization characteristics based on the DIC method, as shown in (b). As shown in (c), the tensile strain field is localized. The propagation path of the tensile crack is approximately perpendicular to the loading direction. The high shear localized zone is mainly concentrated at the junction with the tensile strain field and shear crack. The expansion direction is approximately the same as the loading direction. The tensile crack penetrates along the loading direction by comparing the analyses of (a) and (b). The color change in the localized band of the tensile deformation field is closely related to the size of the crack. In (d), the size of the crack gradually decreases from the upper part to the lower part. The color of the localized zone of the "tensile-shear" strain field in (b) changes from dark to light from top to bottom because of the joint action of the two failure modes of tension and shear. In (a), the size of the crack increases gradually from the top to the bottom. Corresponding to the localized band of tensile strain field in (b), the color changes from light to dark from top to bottom. The shear crack propagates in a direction approximately parallel to the loading direction by comparing the analyses of (e) and (b).

5. Correspondence between Acoustic Emission Characteristics and Deformation Evolution Characteristics

In the process of rock failure, a direct relationship is observed between its internal damage and the evolution of the surface deformation field. The corresponding relationship between the acoustic emission response characteristics and the evolution characteristics of the deformation field is established. The rock instability and failure characteristics are comprehensively studied from the microscopic to the macroscopic level.

5.1. Analysis of Statistical Characteristics

We used MATLAB to normalize the nonuniform deformation index S_w. The acoustic emission cumulative ringing count, emission cumulative energy, cumulative ringing count, acoustic emission cumulative energy, nonuniform deformation index S_w, and the change in stress with time curve are plotted in Figure 9.

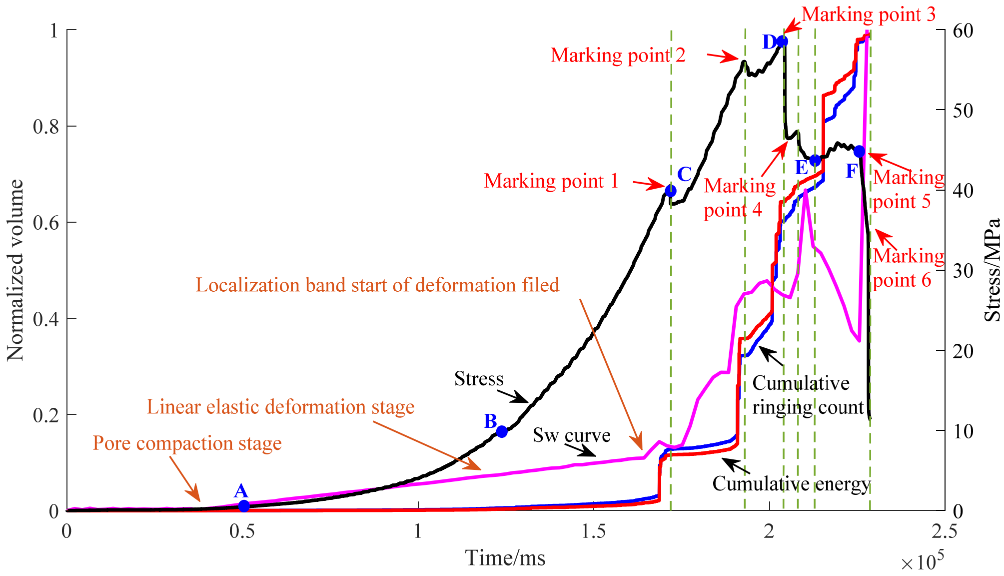

Figure 9. Acoustic emission cumulative ringing count, acoustic emission cumulative energy, nonuniform deformation index and stress change curve with time.

As shown in Figure 10, the S_w curve increases linearly and smoothly with the change in stress at the initial stage of loading (pore compaction stage). The corresponding acoustic emission response characteristics are unremarkable. The accumulated ringing counts and accumulated energy are small, with the linear increase in amplitude. This condition is due to the influence of the compaction of the natural defects inside the rock. Fewer new cracks are observed at this stage in which the specimen has no nonuniform deformation, leading to the slight change in the nonuniform statistical index S_w and the acoustic emission response characteristics. With the increase in stress, the specimen is loaded in the linear elastic deformation stage. The S_w curve increases exponentially with the change in stress, and the corresponding acoustic emission response characteristics are insignificant with a gentle linear increase. At this stage, new microcracks appeared inside the specimen. The microcracks gradually evolved, resulting in a slight change in the acoustic emission response characteristics. However, the rock still had no obvious damage characteristics. Therefore, the nonuniform statistical index S_w and the acoustic emission response characteristics were based on the previous stage. Although an increase occurs, its change is still small. With the continuous increase in stress, the S_w curve, cumulative ringing count curve, and cumulative energy curve at the time of 1.65×10^5 ms showed a turning point for the first time. This condition corresponds to the initiation of a deformation localization zone. After 1.65×10^5 ms, the specimen is loaded in the plastic deformation and failure stage. At this stage, the microcracks gradually evolve into macrocracks and penetrate rapidly. The rock has obvious deformation and failure characteristics, but does not completely lose its bearing capacity, and the corresponding acoustic emission response characteristics are severe. Therefore, the nonuniform statistical index S_w, the accumulative ringing count, and the accumulative energy increase greatly. In the later stage of the stress peak, the specimen enters the residual strength stage. With the gradual decrease in stress, the rock continues to deform and fail, but the failure intensity is significantly reduced, and the corresponding acoustic emission response characteristics are still changing. Therefore, the curve of nonuniform statistical index S_w at this stage is determined. The curve significantly drops, and the cumulative ringing count of acoustic emission and the cumulative energy of acoustic emission continue to increase. When the loading is over, the stress is completely unloaded, and the acquisition of digital images and acoustic emission signals is stopped. The rock is completely destabilized and destroyed, and the deformation degree and acoustic emission response characteristics reach the maximum value. The cumulative energy amount emitted reaches its peak value.

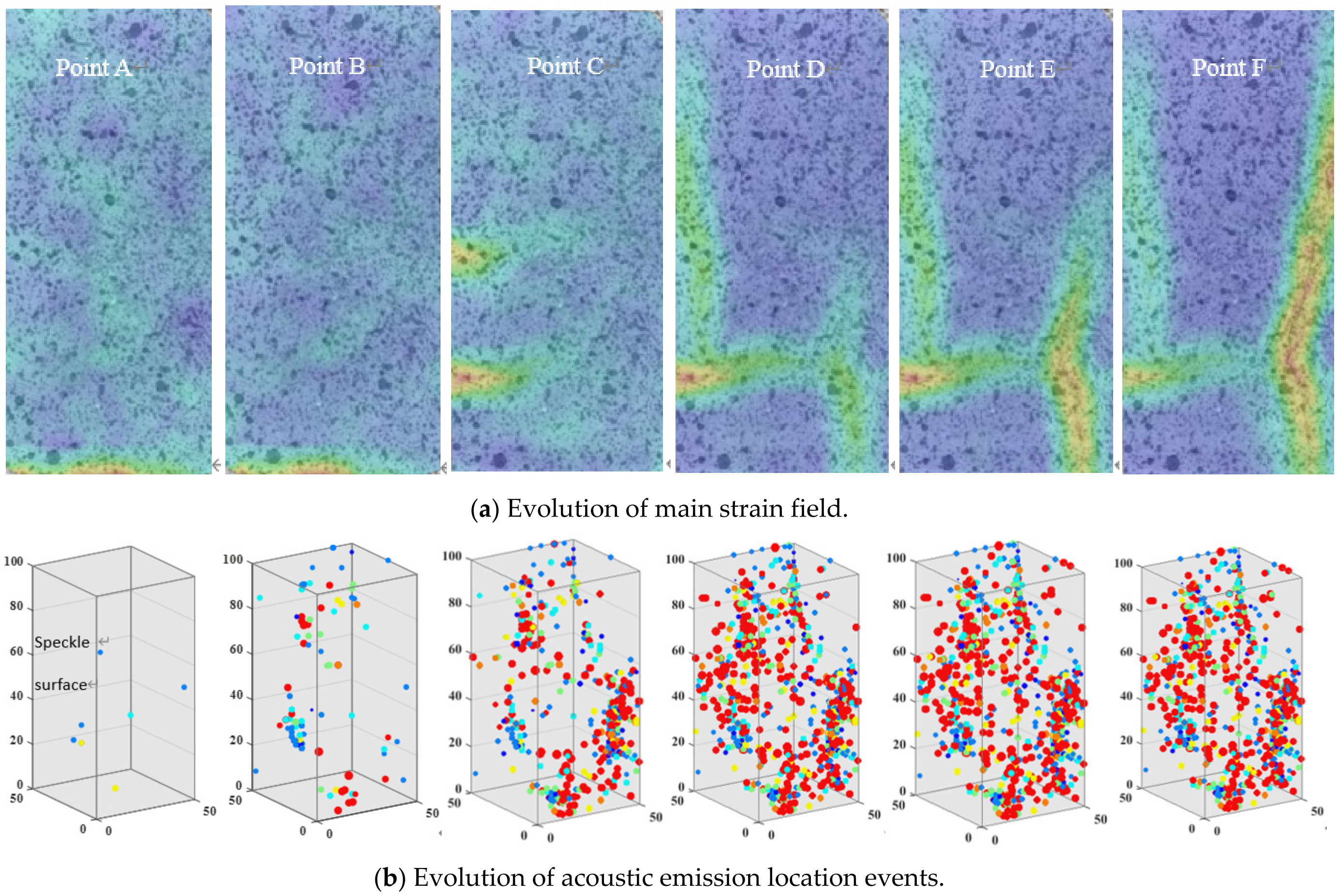

Figure 10. The relationship between the evolution of the main strain field and the variation characteristics of AE events in the whole loading process.

On the basis of the DIC method and the acoustic emission event localization method, the six moments A–E in the total stress–strain curve in Figure 9 are compared and analyzed. The corresponding relationship between the spatial distribution characteristics of acoustic emission localization events and the evolution of the principal strain field is discussed, as shown in Figure 10. A comprehensive analysis of rock instability and failure can be achieved by combining their unique characteristics.

5.2. Analysis of Global Evolution Characteristics

Figure 10 shows the evolution characteristics of the principal strain field and the spatial distribution of acoustic emission localization events corresponding to typical moments in the whole loading process. Figure a shows the evolution characteristics of the principal strain field in the whole process. Figure b shows the evolution characteristics of the spatial distribution of acoustic emission localization events. The speckle surface identified in the first acoustic emission localization event distribution map in Figure b corresponds to the digital image acquisition plane. The six time-points A to E correspond to the points in Figure 9. Time-point A corresponds to the pore compaction stage. Its principal strain field and the spatial positioning point of the acoustic emission event are shown in the figure, where the color of the positioning point reflects the energy of the acoustic emission event. The color changes of red, yellow, blue, cyan, and green indicate that the AE event energy changes from large to small.

As shown in the figure, the pore compaction stage is affected by natural defects inside the rock, and the principal strain field changes slightly. The acoustic emission response is extremely weak, and no obvious acoustic emission localization events are detected. With the increase in stress, the loading process enters the elastic state. In the deformation stage, time B is assigned to the starting point of the linear elastic deformation. At this time, the internal defects are compacted, and the microcracks begin to breed at the local position. The principal strain diagram shows a visible localized band at the bottom of the specimen and the corresponding sound at this time. The spatial positioning points of the emission event increased significantly. From the color of the positioning points, the color at the bottom of the specimen is red, indicating that the acoustic emission energy is large. The positioning events with small energy values are scattered in other parts. The stress continues to increase, and the elastic stage ends. At point C, an obvious deformation localization zone appears in the middle of the specimen, indicating that the microcracks inside the specimen are gradually evolving and penetrating to the middle position. In this case, the number of acoustic emission localization events surges, and the spatial distribution characteristics are consistent with the penetration path of the microcracks. The stress continues to increase and enters the plastic deformation stage. At this stage, the microcracks gradually evolve into macrocracks. The macrocracks gradually penetrate in all directions of the specimen, forcing the specimen to exhibit tensile, shearing, and other failure trends. At time D, the stress reaches its peak value, the macroscopic crack penetrates rapidly in all directions, and the principal strain field has obvious localized bands in the longitudinal and transverse directions and has a tendency to continuously increase. The spatial positioning points of the acoustic emission events continue to surge, mainly concentrated in the crack penetration path. The approximate distribution contour is consistent with the local concentration area of the main strain field. The stress gradually falls back and enters the post-peak deformation failure stage after point D, where macroscopic cracks continue to penetrate. The specimen is seriously unstable and damaged but does not completely lose its bearing capacity.

In addition to point D, the principal strain field at the time of point E continues to evolve on the original basis. The localized zone continues to expand along the same direction. The number of corresponding acoustic emission event spatial positioning points continues to increase, and the spatial distribution continues to accumulate along the same path. The principal strain field in the lower part has obvious change characteristics. The corresponding acoustic emission localization events significantly increase in the lower part. The signal enters the residual strength stage after point E, indicating that the macrocracks have completely penetrated. The failure pattern of the specimen is formed. At time *F*, the specimen is seriously damaged, showing that the main strain field forms a Y-shaped localized band that runs through the entire specimen and expands along the crack path. The strain reaches the maximum value at this moment, and the spatial distribution is also Y-shaped. The stress gradually decreases until it is completely unloaded, and the specimen is completely unstable and damaged after point F. At this stage, the speckle field and the acoustic emission sensor fall off because of the fragmentation of the specimen, making it impossible to calculate the complete principal strain field because of the inability to realize the 3D positioning of the acoustic emission event. In accordance with the above analysis, the evolution characteristics of the principal strain field and the spatial distribution of the acoustic emission event are consistent with the crack propagation and penetration process during the loading and failure process of the specimen. The localized zone and 3D positioning point of acoustic emission event are based on the evolution of the crack propagation path. In the obvious crack part, the principal strain localized zone is in the darker color, indicating that the strain is more concentrated. The number of acoustic emission events and the energy are larger. Figure 10 better reflects the evolution characteristics of the principal strain field and the spatial distribution of acoustic emission events in each stage of the entire loading process. The deformation localization zone and the spatial distribution of the acoustic emission events increase with the increase in stress after the formation of macroscopic cracks. How they transfer and expand with the damage degree and location of the specimen remain to be explored.

6. Dynamic Evolution and Quantitative Description of Specimen Damage

A clustering algorithm was introduced to more accurately describe the damage evolution process of the specimen. The acoustic emission localization results were processed twice to highlight the core area of the damage evolution and to weaken the influence of events with minimal influence on the analysis results.

6.1. Clustering Analysis Algorithm

Density-based spatial clustering of applications with noise (DBSCAN) is a representative density-based clustering algorithm. Different from partitioning and hierarchical clustering methods, the DBSCAN clustering algorithm defines the maximum set of density-connected points as clusters. It can divide regions with sufficiently high density into clusters and can find clusters of arbitrary shapes in noisy spatial databases. As shown in Figure 11, if the data points are divided into three categories, then the core point contains more than the MinPts number of points within the radius Eps. The border point is the number of points within the radius Eps Points that are smaller than MinPts but fall within the neighborhood of the core point. The noise points are neither core points nor boundary points. The concepts of density, reachability, and density connection are proposed to express the density of these points, as shown in Figure 11a.

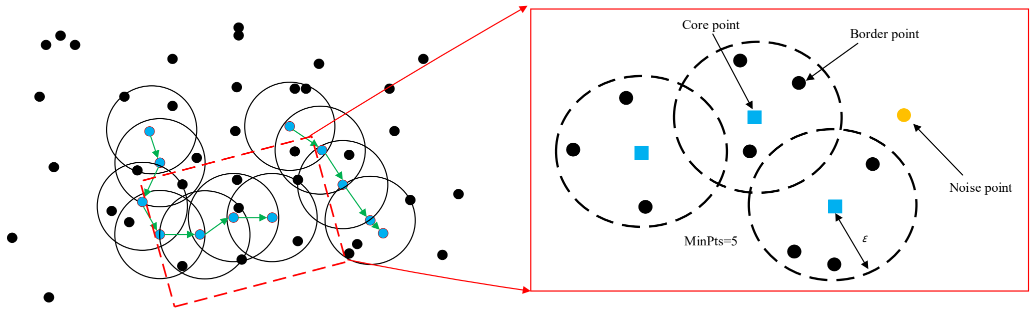

(**a**) Density-related definitions. (**b**) Classification of data points.

Figure 11. Classification and density definition of data points.

The DBSCAN algorithm is used to realize the clustering analysis of acoustic emission events, and the spatiotemporal evolution law and characteristics of acoustic emission events in the process of loading failure are obtained. The occurrence, extension, and penetration of cracks in the specimen are characterized. The key parameters of the algorithm are the number of clustering objects n, the sample number of core objects MinPts, and the neighborhood radius E, where n = 6, MinPts > 5, and E = 3.

The steps of the DBSCAN algorithm can be briefly described as the following steps.

Step 1: choose an initial point. Pick a point arbitrarily, and then find all points where their distance to this point is less than or equal to Eps. If the number of data points within Eps from the starting point is less than min_samples, then the point is marked as noise. If the number of data points within Eps is greater than min_samples, then the point is marked as a core sample and is assigned a new cluster label.

Step 2: visit all neighbors of the point (within distance Eps). If they have not already been assigned a cluster, then assign them a new cluster label created for them. If they are core samples, then visit their neighbors. The cluster grows gradually until no more core samples are found within the Eps distance of the cluster.

Step 3: repeat the above process until the requirements are met. Pick another point that has not been visited and repeat the same process until all points are in the class (core points or edge points) or are peripheral points.

6.2. Analysis of Global Evolution Characteristics

In accordance with the above analysis, the evolution path of the localized zone of the tensile deformation field is parallel to the loading direction, the evolution path of the localized zone of the shear strain field is mostly perpendicular to the loading direction, and the spatial distribution of acoustic emission energy density is consistent with the evolution path of the localized zone. When the localized band is activated, the area of deformation concentration shifts, and the value of the deformation vector gradually decreases. When the new localized zone appears, the original localized zone continues to evolve and gradually forms, the value of the variable vector gradually decreases, and the deformation value of the new localized zone gradually increases. The deformation value of the remaining deformation regions is approximately zero after the deformation localization zone is formed. When the specimen is damaged along a localized zone, the deformation value of the remaining localized zones decreases rapidly. After the specimen is damaged, the deformation value of the remaining localized failure zones increases again until the specimen is completely unstable. The acoustic emission energy density is displayed in 3D form, and its variation law is closely related to the rock's failure evolution process. However, its spatial distribution law cannot be completely consistent with the evolution characteristics of the plane localized zone, and certain differences are observed. Therefore, the acoustic emission data must be further processed from a 2D perspective to study the coupling relationship between its distribution characteristics and the evolution of the deformation localization zone, as shown in Figure 12.

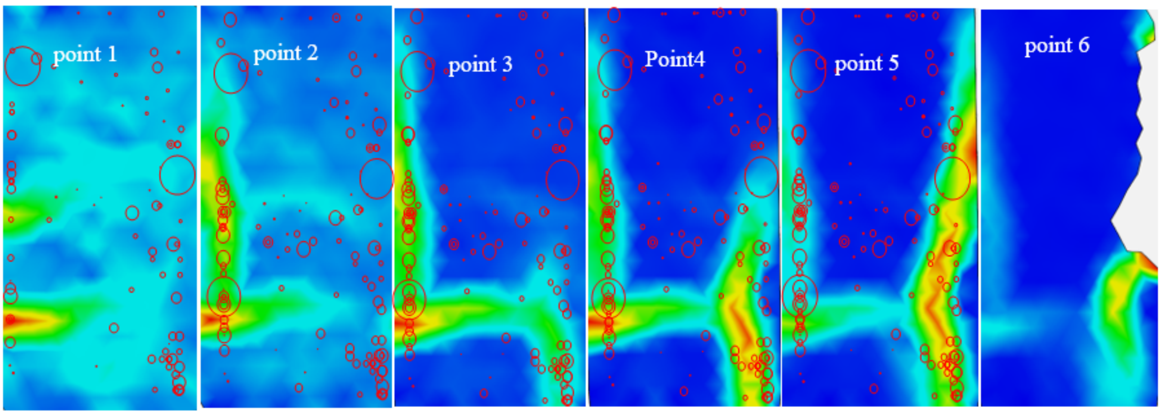

Figure 12. Superimposed evolution characteristics of deformation field localization band and acoustic emission localization event.

The acoustic emission data are clustered and processed by using the DBSCAN clustering algorithm. Only the acoustic emission localization within the path range of the deformation localization zone is analyzed to more intuitively reflect the coupling relationship between the spatial distribution characteristics of the acoustic emission localization events and the deformation localization zone. The event is projected in the 2D plane and superimposed with the deformation field image, and the final display effect is shown in Figure 12. The figure shows that the shape and size of the cluster symbols represent the energy size of the microseismic event, and the larger the shape, the larger the energy, and vice versa.

The clustering results show that the distribution law of such events is consistent with the evolution path of the localized zone. The distribution law plays a decisive role in the failure and instability of rock. At the time of point 1, the localized zone 1 is activated. The deformation value of the deformation field is then increased. The clustering results of the acoustic emission events are mainly concentrated on two sides of the specimen, but the middle part is scattered. The acoustic emission event gradually expands to the middle part. When the localized zone 2 starts, the acoustic emission event on the left side of the specimen increases significantly and distributes along the path of the localized zone 2. When the evolution of zone 2 is completed, the acoustic emission events continue to increase and induce the activation of localized zone 3, in which the acoustic emission localization events on the right side of the specimen increase. The deformation value of localized zone 2 gradually decreases. The acoustic emission localization events continue to increase in this stage and scattered along the path of localized zone 3 near localized zone 3. At the time of point 6, the localized specimen is damaged along localized zone 3. The deformation values of localized zones 1 and 2 are approximately zero. Such results are the same as those described above. The acoustic emission sensor falls off, and the effective acoustic emission signal cannot be collected because of the damage to the specimen. Therefore, locating the acoustic emission event is impossible.

7. Conclusions

In this study, the dynamic failure test of standard rock specimens under uniaxial loading is performed. The data of rock deformation images and acoustic emission signals are collected by using a CCD camera and a DS5-8B full-information acoustic emission instrument. Combined with the acoustic emission signal analysis method and the DIC method, the failure and instability process of rock is studied in depth, and the coupling relationship between the deformation field evolution and the acoustic emission response characteristics is discussed. The preliminary conclusions are summarized as follows:

(1) A good correspondence is observed between the loading stress and acoustic emission response characteristics. When the stress mutates (surges or suddenly decreases), the cumulative ringing count and cumulative energy of the acoustic emission increase sharply. The accumulative ringing count of the acoustic emission and the cumulative energy of acoustic emission surge, whereas the stress does not necessarily change.

(2) The evolution characteristics of the deformation field are closely related to the acoustic emission response characteristics. The larger the deformation value, the more intensive the acoustic emission location events, and the greater the acoustic emission energy. The acoustic emission location events are clustered by using the DBSCAN algorithm. The clustering results show that the spatial evolution path of some acoustic emission events is consistent with the evolution path of the deformation localization zone.

(3) The evolution path of the deformation localization band is consistent with the coalescence path of the crack. The evolution direction of the tensile deformation localization band is perpendicular to the loading direction, and the evolution direction of the shear deformation localization band is approximately parallel to the loading direction. When the new localized band appears, the existing localized band evolves continuously, and the deformation value decreases gradually. The deformation value of the deformation field is closely related to the initiation and evolution of the deformation localization zone. After the formation of the localization zone, the deformation value of the other regions of the deformation field is approximately zero.

Author Contributions: Writing—original draft, Q.Z., E.Z., Z.Y. and L.S.; funding acquisition, Z.Y. and Q.Z.; writing—review and editing, Z.Y., L.S. and Y.Y.; methodology, Q.Z., E.Z. and Y.Z.; software, Q.Z., E.Z. and Y.Z.; data acquisition, Y.Y., L.S. and L.G.; supervision, Z.Y. and Q.Z. All authors have read and agreed to the published version of the manuscript.

Funding: The authors gratefully acknowledge financial support from the National Key Research and Development Program of China (No. 2021YFC3090403), the central government guides local science and technology development fund project (No. 216Z5401G), the S&T Program of Hebei (No. 22375401D), the Fundamental Research Funds for the Central Universities (No. 3142021002), and the scientific research program of the colleges and universities in Hebei Province (No. Z2020124).

Institutional Review Board Statement: Not applicable.

Informed Consent Statement: Not applicable.

Data Availability Statement: Not applicable.

Conflicts of Interest: The authors declare no conflict of interest.

References

1. Yang, Y.; Xiong, B.; Peng, S.; Liu, S.; Chen, H.; Zhang, T. Transient electromagnetic characteristics of coal seams intruded by magmatic rocks. *PLoS ONE* **2022**, *17*, e0263293. [CrossRef] [PubMed]
2. Xue, J.; Chen, Z.; Li, Y.; Wang, J.; Li, X. Failure characteristics of coal-rock combined bodies based on acoustic emission signals. *Arab. J. Geosci.* **2022**, *15*, 135. [CrossRef]
3. Bu, F.; Xue, L.; Zhai, M.; Huang, X.; Dong, J.; Liang, N.; Xu, C. Evaluation of the characterization of acoustic emission of brittle rocks from the experiment to numerical simulation. *Sci. Rep.* **2022**, *12*, 498. [CrossRef] [PubMed]
4. Liu, X.; Han, M.; Li, X.; Cui, J.; Liu, Z. Elastic wave attenuation characteristics and relevance for rock microstructures. *J. Min. Sci.* **2020**, *56*, 216–225. [CrossRef]
5. Zhao, Y.; Li, B.; Zhang, C.; Cheng, C. Experimental study on charge induction and microseismic laws of coal and rock with different combination ratios. *J. Saf. Sci. Technol* **2019**, *15*, 107–112.
6. Li, J. Research on the application of acoustic emission intelligent monitoring and early warning technology for the coal-rock dynamic disasters in underground mining faces. In *IOP Conference Series: Earth and Environmental Science*; IOP Publishing: Bristol, UK, 2020; Volume 526, p. 012121.
7. Zhang, G.; Li, H.; Wang, M.; Li, J.; Deng, S. Comparative study on damage characterization and damage evolution of rock under uniaxial compression. *Chin. J. Geotech. Eng.* **2019**, *41*, 1074–1082.
8. Zuo, J.; Pei, J.; Liu, J.; Peng, R.; Li, Y. Investigation on acoustic emission behavior and its time-space evolution mechanism in failure process of coal-rock combined body. *Chin. J. Rock Mech. Eng.* **2011**, *30*, 1564–1570.
9. Li, S.; Yin, X.; Wang, Y.; Tang, H. Studies on acoustic emission characteristics of uniaxial compressive rock failure. *Chin. J. Rock Mech. Eng.* **2004**, *23*, 2499–2503.
10. Ma, Z. Exploration on adaptive digitalfilting of site noise in rock ae test. *Chin. J. Rock Mech. Eng.* **1999**, *6*, 685–689.
11. Zhang, W.; Xingping, L.; Tao, Q.; Jiang, D.; Zhang, G.; Ying, T. Acoustic emission monitoring for dynamic destabilization of heavy and steep coal seam. *J. Xi'an Univ. Sci. Technol.* **2011**, *31*, 253–255.
12. Wang, E.; Liu, X.; He, X.; Li, Z. Acoustic emission and electromagnetic radiation synchronized monitoring technology and early-warning application for coal and rock dynamic disaster. *J. China Univ. Min. Technol.* **2018**, *47*, 942–948.
13. Zhou, Y.; Wu, S.; Xu, X.; Sun, W.; Zhang, X. Particle flow analysis of acoustic emission characteristics during rock failure process. *Chin. J. Rock Mech. Eng.* **2013**, *32*, 951–959.
14. Liu, F.; Yang, T.; Zhang, P.; Zhou, J.; Deng, W.; Hou, X.; Zhao, Y. Dynamic inversion of rock fracturing stress field based on acoustic emission. *Rock Soil Mech.* **2018**, *39*, 1517–1524.
15. Shang, J.; Hu, J.; Zhou, K. Numerical tests on heterogeneous effect in damage and acoustic emission characteristic of rocks under uniaxial loading. *J. Cent. South Univ. Sci. Technol.* **2013**, *44*, 2470–2475.
16. Hassan, G.M. Deformation measurement in the presence of discontinuities with digital image correlation: A review. *Opt. Lasers Eng.* **2021**, *137*, 106394. [CrossRef]
17. Song, H.; Zhao, Y.; Elsworth, D.; Jiang, Y.; Wang, J. Anisotropy of acoustic emission in coal under the uniaxial loading condition. *Chaos Solitons Fractals* **2020**, *130*, 109465. [CrossRef]
18. Alam, S.Y.; Saliba, J.; Loukili, A. Fracture examination in concrete through combined digital image correlation and acoustic emission techniques. *Constr. Build. Mater.* **2014**, *69*, 232–242. [CrossRef]
19. Uzun, F.; Korsunsky, A.M. The height Digital Image Correlation (hDIC) technique for the identification of triaxial surface deformations. *Int. J. Mech. Sci.* **2019**, *159*, 417–423. [CrossRef]
20. Lin, L.-x.; Xu, M.-j.; Xu, J.-j.; Lu, H.; Ye, C.-h.; Yu, C.; Chen, J.-m. Measurement and evaluation of strain fields in T23 steel based on digital image correlation method. *J. Cent. South Univ.* **2017**, *24*, 1977–1985. [CrossRef]
21. Munoz, H.; Taheri, A.; Chanda, E. Pre-peak and post-peak rock strain characteristics during uniaxial compression by 3D digital image correlation. *Rock Mech. Rock Eng.* **2016**, *49*, 2541–2554. [CrossRef]
22. Munoz, H.; Taheri, A. *Postpeak Deformability Parameters of Localized and Nonlocalized Damage Zones of Rocks under Cyclic Loading*; ASTM International: West Conshohocken, PA, USA, 2018.
23. Ma, Y.; Chen, W.; Yang, D.; Yang, J.; Gong, Z. Experimental study of brittle rock failure based on three-dimensional digital image correlation technique. *Rock Soil Mech.* **2017**, *38*, 117–123.
24. Zhu, Q.; Li, D.; Han, Z.; Li, X.; Zhou, Z. Mechanical properties and fracture evolution of sandstone specimens containing different inclusions under uniaxial compression. *Int. J. Rock Mech. Min. Sci.* **2019**, *115*, 33–47. [CrossRef]
25. Zhao, J.; Yin, L.; Guo, W. Influence of three-dimensional roughness of rock fracture on seepage characteristics based on the digital image technology. *Arab. J. Geosci.* **2018**, *11*, 778.
26. Zhao, C.; Tian, J.; Matsuda, H.; Zhao, C.; Bao, C. Crack propagation and damage of rock under uniaxial compression based on global strain field analysis. *Chin. J. Rock Mech. Eng.* **2015**, *34*, 763–769.
27. Hu, X.; Gong, X.; Hu, H.; Guo, P.; Ma, J. Cracking behavior and acoustic emission characteristics of heterogeneous granite with double pre-existing filled flaws and a circular hole under uniaxial compression: Insights from grain-based discrete element method modeling. *Bull. Eng. Geol. Environ.* **2022**, *81*, 162. [CrossRef]

28. Song, Y.; Ma, S.; Yang, X.; Wang, X. Experimental investigation on failure of rock by digital speckle correlation methods. *Chin. J. Rock Mech. Eng.* **2011**, *30*, 170–175.
29. Pan, B.; Qian, K.; Xie, H.; Asundi, A. Two-dimensional digital image correlation for in-plane displacement and strain measurement: A review. *Meas. Sci. Technol.* **2009**, *20*, 062001. [CrossRef]